

*Intraseasonal variability of winter precipitation over Central Asia and the Western Tibetan plateau from 1979 to 2013 and its relationship with the North Atlantic Oscillation*

Article

Accepted Version

Creative Commons: Attribution-Noncommercial-No Derivative Works 4.0

Liu, H., Liu, X. and Dong, B. ORCID: <https://orcid.org/0000-0003-0809-7911> (2017) Intraseasonal variability of winter precipitation over Central Asia and the Western Tibetan plateau from 1979 to 2013 and its relationship with the North Atlantic Oscillation. *Dynamics of Atmospheres and Oceans*, 79. pp. 31-42. ISSN 0377-0265 doi: <https://doi.org/10.1016/j.dynatmoce.2017.07.001> Available at <https://centaur.reading.ac.uk/73198/>

It is advisable to refer to the publisher's version if you intend to cite from the work. See [Guidance on citing](#).

Published version at: <https://doi.org/10.1016/j.dynatmoce.2017.07.001>

To link to this article DOI: <http://dx.doi.org/10.1016/j.dynatmoce.2017.07.001>

Publisher: Elsevier

All outputs in CentAUR are protected by Intellectual Property Rights law, including copyright law. Copyright and IPR is retained by the creators or other copyright holders. Terms and conditions for use of this material are defined in

the [End User Agreement](#).

[www.reading.ac.uk/centaur](http://www.reading.ac.uk/centaur)

## **CentAUR**

Central Archive at the University of Reading

Reading's research outputs online



---

23 of the 500 hPa geopotential height anomalies over the southern and northern North Atlantic  
24 10 days earlier (at 95% significance level), that bear a similarity to the North Atlantic  
25 Oscillation (NAO). The composite analysis revealed that the NAO impacts the downstream  
26 regions including CAWTP by controlling south-north two branches of the middle latitude  
27 westerly circulation around the Eurasian border. During the positive phases of the NAO, the  
28 northern branch of the westerly circulation goes around the northwest Tibetan Plateau,  
29 whereas the southern branch encounters the southwest Tibetan Plateau, which leads to a  
30 reduced precipitation over the northern Pamir Plateau and an increased precipitation over  
31 the Karakoram Himalaya, and vice versa.

32 KEY WORDS: Topographic precipitation; North Atlantic Oscillation; Westerly circulation;  
33 Statistical analysis; Intraseasonal variability.

34

## 35 **1 Introduction**

36 The geographical region covered by Central Asia and the western Tibetan Plateau (CAWTP,  
37 30–45° N, 60–85° E) has complex terrains and a unique climate. The Turan Depression is  
38 located in the northwest, whereas the high mountains and plateaus (e.g. the Iran Plateau, the  
39 Hindu Kush, the Karakoram Himalaya, the Pamir Plateau and the Tian Shan mountains) are  
40 located from the southwest to the northeast (Fig. 1). The CAWTP region has an arid to semiarid  
41 climate with an annual precipitation less than 400 mm, except for a few of the high mountain  
42 areas. Because of the scarcity of water resources, there is a high risk that global climate change  
43 will threaten both the natural environment and the human population in this region (Ragab &

---

44 Prudhomme 2002, WB et al. 2009).

45 Despite the complex topography and lack of meteorological stations, satellite remote  
46 sensing data have been used to determine the spatiotemporal distribution of precipitation  
47 over Central Asia (Guo et al. 2015) and the western Tibetan Plateau (Pohl et al. 2015). High-  
48 resolution regional climate models have also been used to determine the patterns of  
49 precipitation over CAWTP (Small et al. 1999, Schiemann et al. 2008, Ozturk et al. 2012,  
50 Maussion et al. 2014).

51 Previous studies have reported the spatiotemporal distribution and regional differences  
52 in precipitation over CAWTP and have found that the major weather system controlling the  
53 winter precipitation over CAWTP is the westerly circulation (Schiemann et al. 2009, Yin et al.  
54 2014). In winter, the westerly circulation transports moisture to Central Asia (Bothe et al.  
55 2012), southwest Asia (Malik et al. 2015) and the western Tibetan Plateau (Curio et al. 2015).  
56 The westerly circulation is disturbed by the high mountains in this region and causes heavy  
57 precipitation and storms over the Pamir Plateau, the Hindu Kush, the Karakoram Himalaya and  
58 the western Himalaya (Lang & Barros 2004, Cannon et al. 2015a, b). Yin et al. (2014) compared  
59 the differences in precipitation climatology between the arid area of Central Asia and the East  
60 Asia monsoon region and showed that winter is the rainy season in Central Asia, whereas the  
61 rainy season occurs in summer for East Asia. They further showed that the control  
62 atmospheric circulation over the western area changes between winter and summer. In winter  
63 it is dominated by westerly upper-air flows, bringing moisture from the upstream to the region  
64 while in summer it is dominated by northeasterly winds from the Asian interior, resulting in a

---

65 dry condition. The westerly circulation is not only the major weather system controlling the  
66 winter mean precipitation over CAWTP, but also precipitation interannual variability and trend  
67 in the region (Chen et al. 2011, Yin et al. 2014, Cannon et al. 2015a).

68 There have been many reports that large-scale atmospheric teleconnections regulate the  
69 mid-latitude westerly circulation variability which in turn may influence interannual  
70 precipitation variation over CAWTP (e.g. Aizen et al. 2001, Syed et al. 2006, Mariotti 2007,  
71 Filippi et al. 2014, Yin et al. 2014, Cannon et al. 2015a, b, Hoell et al. 2015). Although some  
72 evidence has been found that at interannual time scale the El Niño–Southern Oscillation may  
73 be related to the precipitation variation in the cold season over Central and Western Asia  
74 (Mariotti 2007, Hoell et al. 2015), other research has shown a close relationship between the  
75 winter interannual precipitation variation over CAWTP and the North Atlantic Oscillation (NAO)  
76 (Aizen et al. 2001, Syed et al. 2006, 2010, Yadav et al. 2009, Filippi et al. 2014, Yao and Chen  
77 2015). Aizen et al. (2001) analyzed the relationship between mid-latitude precipitation in Asia  
78 and the large-scale circulation of the atmosphere using data from hydro-meteorological  
79 stations. Their results showed more precipitation over the Pamir and Tian Shan mountains  
80 during the positive phases of the NAO. Syed et al. (2006) found a positive precipitation  
81 anomaly over northwestern Asia that is well matched with the positive phase of the NAO.  
82 Syed et al. (2010) presented a regional climate modeling study on both NAO and ENSO and  
83 discussed the influence of westerly disturbances. Filippi et al. (2014) verified that winter  
84 interannual precipitation variation over the Hindu Kush–Karakoram Himalaya region is  
85 affected by the NAO. During the positive phases of the NAO, the Middle East, which is

---

86 upstream of CAWTP, experiences stronger westerly winds and evaporation, which leads to an  
87 enhanced moisture transport and therefore enhanced precipitation over the Hindu Kush. Yao  
88 and Chen (2015) found a significant negative correlation between the yearly precipitation on  
89 mountains of the Syr Darya River Basin and NAO index from 1891 to 2011 but it turned out  
90 non-significant on plains.

91 Previous studies have mainly considered the interannual variation in winter precipitation  
92 over a specific area and its connection with the NAO and other large-scale circulations (e.g.  
93 Aizen et al. 2001, Syed et al. 2006, Mariotti 2007, Filippi et al. 2014, Yin et al. 2014, Cannon et  
94 al. 2015a, Hoell et al. 2015). However, little attention has been paid to the spatiotemporal  
95 distribution of precipitation variability over CAWTP at the intraseasonal time scale. Therefore  
96 it is important to investigate the spatial and temporal distribution of winter precipitation  
97 variation over CAWTP on this time scale, to analyze its connection with regional and large-  
98 scale circulations and to elucidate physical processes involved by using daily precipitation data  
99 and other meteorological parameters.

100

## 101 **2 Data and methods**

102 Daily precipitation data from the Climate Prediction Center (Chen et al. 2008) and daily  
103 meteorological variables of ERA-Interim from the European Centre for Medium-Range  
104 Weather Forecasts (Dee et al. 2011) were used in this study. Sapna Rana (2017) have already  
105 used the CPC Unified Rain gauge data and compared it with 9 other precipitation products  
106 over the central southwest Asia. Their results show that the CPC data can reasonably reflect

---

107 the spatial-temporal distribution of winter precipitation over CAWTP despite some systematic  
108 differences in the time means The used ERA-Interim variables include the daily 700 and 500  
109 hPa geopotential height, meridional and zonal winds, the total column of water vapor (TCWV)  
110 and the mean sea level pressure. The horizontal resolution of all the data is  $0.5^\circ$  longitude  $\times$   
111  $0.5^\circ$  latitude. In consideration of the higher accuracy of the reanalysis data obtained over high  
112 mountain areas after 1979, when satellite data were first applied (Cannon et al. 2015b), we  
113 chose all winters (December-March), consistent with other studies analyzing the relationships  
114 between teleconnection patterns and precipitation in this area (Syed et al. 2006, 2010, Yadav  
115 et al. 2009, Filippi et al. 2014) from 1979 to 2013, a total of 4244 days, as the study period.  
116 The daily average data were obtained from four records with a six-hour interval for each day.  
117 The encounter of westerly wind with high mountains of Tibetan Plateau happened around  
118 700 hPa , which is closely connected with topographic precipitation, and therefore 700 hPa  
119 wind is used to indicate low tropospheric circulation. The 500hPa geopotential height anomaly  
120 can indicate the teleconnections.

121 To determine the characteristics of the winter intraseasonal precipitation and circulation  
122 variability in CAWTP, the climatological seasonal cycle from December to the next March in  
123 the daily data was removed before the analysis. We averaged the data of the same date of all  
124 the years (1979-2013) and then calculated the 21 day moving mean as the climate mean state.  
125 Thus, the daily values with climatological seasonal cycle removed were obtained by  
126 subtracting the climate mean state from the actual data according to the following formula:

$$127 \quad Z_n^* = Z_n - \left( \sum_{i=-10,10} \left( \sum_{j=1,35} Z_{k+(i-1)\times 365+j} \right) / 35 \right) / 21$$

---

128 where  $n$  is the number of days from December 1, 1979;  $k$  is the number of days from  
129 December 1 of a specific year;  $i$  is the number of years from 1979;  $j$  is the day from 10 days  
130 before to 10 days after a specific day; and  $Z_n^*$  is the value after removing the climatological  
131 seasonal cycle.

132 The EOF analysis was used to decompose winter daily precipitation variability over  
133 CAWTP to find the spatial patterns as well as their time variation (Bjornsson and Venegas  
134 1997). Figure 1 shows the study area with 1581 grid boxes and 4244 day time series at each  
135 grid box, which is the basis for the EOF analysis.

136 Singular value decomposition (SVD) analysis (Wallace et al. 1992) was applied to show  
137 the spatiotemporal relationship between the winter daily precipitation and the regional  
138 circulation variations over CAWTP. This method identifies a pair of covaried spatial patterns,  
139 their temporal variations and the covariance between two variables (Bjornsson and Venegas  
140 1997).

141 Lead-lag linear regression was applied to study the connection between the 500 hPa  
142 geopotential height variability over CAWTP and the upstream westerly jet variability (Wang  
143 and Zhang 2015).

144 We also constructed composites of the precipitation distribution in CAWTP during  
145 positive and negative NAO cases respectively, and discussed the relationship between the  
146 NAO and the precipitation variability at the intraseasonal time scale. The NAO index was  
147 defined as the standardized difference in mean sea level pressure between the southern  
148 North Atlantic (25°–40°N, 50°–10°W) and the northern North Atlantic (50°–65°N, 10°–50°W)

---

149 (Hurrell 1996). After calculating the daily index for every winter from 1979 to 2013, the central  
150 day of a positive (negative) NAO phase event was defined as the day with the relative  
151 maximum (minimum) value of the NAO index in continuous five days and being greater (less)  
152 than 1.5 (-1.5) at the same time. In this way, a total of 85 positive NAO phase cases and 82  
153 negative phase cases were selected for the composites. Here we did composite analysis  
154 based on cases with strong NAO anomalies in order to see teleconnections between two  
155 regions and significant NAO related remote climatic anomalies over CAWTP. To trace westerly  
156 wind disturbance (WWD) tracks, a wave-tracking approach was applied as documented in  
157 Cannon (2015b) who defined the centers of the disturbances by standardized 500 hPa  
158 geopotential height anomaly and a set of spatial threshold and temporal correlation to  
159 identify the tracks. Here we used the 500hPa geopotential height anomaly of 1 standard  
160 deviation and the spatial extent of 5 degrees as a set of thresholds to identify the location of  
161 centers to count the WWDs. Then the WWD frequency in every grid was calculated.

162

### 163 **3 Spatial and temporal distribution of winter precipitation over CAWTP and its connection** 164 **with the contemporaneous regional circulation**

#### 165 3.1 Winter precipitation climatology over CAWTP

166 The climate of Central Asia is controlled on an annual basis by westerly winds containing  
167 little moisture, and it is classified as a typical arid to semiarid region. The rainy season usually  
168 occurs in winter (from December to March) (Yin et al. 2014) and most of the moisture  
169 transported by the strong westerly winds is intercepted to condense by the high mountains

---

170 of the region during this period (Syed et al. 2006). Figure 2a shows the spatial distribution of  
171 the winter mean climatological precipitation over Asia from 1979 to 2013. There is more  
172 precipitation over CAWTP and the main areas of precipitation are distributed on the windward  
173 slope of the western Tibetan Plateau, in agreement with earlier reports by Schiemann et al.  
174 (2008) and Yin et al. (2014). There are two core areas of precipitation centered at 70°E, 42°N  
175 and 75°E, 33°N respectively, with the maximum precipitation rate of 8 mm d<sup>-1</sup>. The winter  
176 precipitation over CAWTP accounts for more than 50% of the annual precipitation (Fig. 2b).  
177 The distribution of water vapor flux integrated vertically from 950 hPa to 300 hPa (Fig. 2c)  
178 suggests that the moisture transport convergence over CAWTP is mainly controlled by mid-  
179 tropospheric westerly winds, rather than by lower-tropospheric (below 950 hPa) circulations  
180 (not shown). The distribution of WWD frequency (Fig. 2d) shows that more WWDs occur in  
181 the Karakoram Himalaya, coincident with the local precipitation maximum there shown in Fig.  
182 2a. This is consistent with Cannon et al. (2015a, b) who reported that heavy precipitation  
183 occurs when the WWD encountered mountains of the Himalaya. The climatology of  
184 precipitation over CAWTP is quite different from that over the monsoon areas. The annual  
185 precipitation over CAWTP is much lower than that over Asian monsoon regions and mainly  
186 occurs in winter, when the mountains block and lift the strong mid-latitude westerly  
187 circulation (e.g., Yin et al 2014, Cannon et al. 2015a, b).

### 188 189 3.2 Intraseasonal variability in winter daily precipitation and circulation over CAWTP

190 It is possible that the strength and position of westerly circulation determine the forced

---

191 upward motion, frequency of WWDs and the distribution of precipitation on the intraseasonal  
192 time scale. The winter daily precipitation was decomposed by EOF analysis after the  
193 climatological seasonal cycle was removed and the first two modes are shown in Fig. 3a and  
194 3b. The first mode shows the same sign all over CAWTP with explained variance of 24.4% and  
195 the second mode shows a seesaw pattern between northern Pamir Plateau and the  
196 Karakoram Himalaya with explained variance of 15.6%. These EOF modes suggest the  
197 existence of the intraseasonal variability of winter precipitation over CAWTP. Then we  
198 composited the 500 hPa zonal wind (U component) during the dominant periods according to  
199 the time series of the first mode and the second mode as Fig. 3c and Fig. 3d, which indicated  
200 close connection between regional circulation and precipitation. Therefore, the relationship  
201 between the regional circulation and precipitation in the study area is explored in the  
202 following.

203         The seasonal cycle removed daily precipitation and 700hPa moisture flux fields for 35  
204 winters during 1979–2013 were used for the SVD analysis to determine the simultaneous  
205 relationship between the precipitation and circulation variability over CAWTP. The first SVD  
206 mode shows a dipole pattern of precipitation variability with a positive anomaly over the  
207 Karakoram Himalaya (center located at 33°N, 78°E, Fig.4a) and a negative anomaly over the  
208 northern Pamir Plateau (center located at 40°N, 68°E), bearing a very similar structure as  
209 shown for the second mode of EOF analysis (Fig. 3b). Accompanied with this pattern of  
210 precipitation variability is a southerly wind anomaly over the Karakoram Himalaya and a  
211 northwesterly wind anomaly (southwesterly wind weakened) over the northern Pamir

---

212 Plateau(not shown) and anomalous lower tropospheric moisture transport (Fig. 4b). This  
213 pattern of precipitation anomaly is closely related to the forced lifting of the westerly  
214 airstream on the windward side of the mountains. The explained variance reaches 55.12% and  
215 the correlation coefficient between the time coefficients of two fields is 0.65 for the first SVD  
216 mode, suggesting the importance of orographic forcing in modulating the regional  
217 precipitation at the intraseasonal time scale.

218 We also did the SVD analysis with the seasonal cycle removed daily precipitation and 500  
219 hPa geopotential height fields over CAWTP. The explained variance and correlation coefficient  
220 corresponding for the first SVD mode are 60.5% and 0.64, respectively (Fig. 4c and d). Figs. 4c  
221 and 4d illustrate that a negative center over the southeast of CAWTP in the field of 500 hPa  
222 geopotential height anomaly is associated with a precipitation anomaly pattern with the  
223 wetter southeast and the drier northwest. Hence, the distribution of winter precipitation  
224 anomaly in the study area at the intraseasonal time scale is the result of topography-affected  
225 regional atmospheric circulation variability. In the following, a lead-lag linear regression was  
226 used to further reveal the relationship between the regional and large-scale circulation  
227 variations and the regional precipitation change.

228

#### 229 **4 Correlation of 500hPa geopotential height over CAWTP with the preceding atmospheric** 230 **circulation over the North Atlantic Ocean and Eurasia**

231 The preceding atmospheric circulation over the Atlantic Ocean and Eurasian region may  
232 influence the regional circulation over CAWTP, leading to the regional precipitation anomaly

---

233 via teleconnection. The time series of the 500 hPa geopotential height analyzed by SVD was  
234 normalized and then the normalized time series with an absolute value greater than 1.5 and  
235 higher than the neighboring 4 other days was chosen for further analysis (a total of 200 time  
236 series mixed with both positive and negative values). A linear regression was applied between  
237 the chosen 200 time series and the antecedent 500 hPa geopotential height field over the  
238 Atlantic Ocean–Eurasian region from lead 16 days to the lag 3 day of the chosen days  
239 respectively and results are shown in figure 5. There is a positive geopotential height anomaly  
240 over the Azores (center located at 30°W and 40°N) and a negative anomaly over Iceland  
241 (center located at 10°W and 60°N) from day –10 to day –8 (10 to 8 days before the regional  
242 circulation phase, the same below) (Fig. 5a, 5b). These patterns of the anomalous circulation  
243 show a similarity to the positive phase of the NAO (Hurrell 1996). On day –6, the original  
244 negative geopotential height anomaly over Iceland moves to the east and a significant positive  
245 anomaly occurs over the Eurasian border and northern Asia and meanwhile a negative  
246 anomaly over CAWTP develops (Fig. 5c). With time advance, the magnitude of the anomaly  
247 over the Atlantic Ocean decrease, whereas the strength of the anomalies over the Eurasian  
248 border and over CAWTP enhance on day –4 (Fig. 5d). On day –2 and 0, significant negative  
249 geopotential height anomalies occur over CAWTP (Fig. 5e, 5f), similar to the results of the SVD  
250 analysis. It is therefore possible that the regional circulation has been affected by the  
251 preceding large-scale circulation variability related to NAO.

252 The time evolution of the 500hPa geopotential height anomaly over the North Atlantic  
253 was analyzed by lead-lag linear regression and correlation. Areas A (20–40° W, 30–40° N), B

---

254 (0–20° W, 54–64° N), C (44–64° E, 54–64° N) and D (60–80° E, 30–40° N) in Fig. 5 were chosen  
255 to calculate the average geopotential height anomaly and the correlation coefficient in  
256 different lead days. The four domains are recognized in consideration of both covering the  
257 centers of 500hPa geopotential height anomaly and the significant at 95% level in Fig. 5.  
258 Otherwise, the numbers of the grids of the four domains should be the same so they are  
259 comparable. Table 1 lists regression coefficients and correlation coefficients of regionally-  
260 averaged 500 hPa geopotential heights on different lag days for these four areas and the time  
261 coefficients of the first mode of 500 hPa geopotential height field over CAWTP in the above  
262 SVD analysis. From days –15 to –9 (the negative number means the days before the day for  
263 the regional SVD analysis) there is a positive anomaly over area A, a significant increasingly  
264 negative anomaly over area B, and no significant anomaly over area C. From days –8 to –4,  
265 the anomaly over area A decreases and the anomaly over area B increases to a maximum  
266 value. A significant positive anomaly appears over area C on day –5 and increases rapidly  
267 afterwards. From days –3 to 0 there is no significant anomaly over area A, the anomaly over  
268 area B decreases, and the anomaly over areas C and D increases to maximum values. From  
269 days +1 to +3 there is no significant anomaly over area B and the anomaly over areas C and D  
270 decreases. Figure 5 and Table 1 show time evolutions of geopotential height anomaly in  
271 various regions before the maximum height anomaly over CAWTP and suggest that NAO-like  
272 circulation anomaly over the North Atlantic is a precursor for the intraseasonal variation of  
273 precipitation over CAWTP. The lead-lag correlation coefficients between NAO index and time  
274 series of first SVD mode in these chosen days were calculated and they are given in Table 1.

---

275 These correlation coefficients indicate large correlations when NAO leads the regional  
276 geopotential height by about 10 days.

277 Although we found a close connection between the 500 hPa geopotential height over  
278 CAWTP and geopotential height over the North Atlantic about 10-8 days before by linear  
279 regression and correlation, further analysis was required to elucidate the mechanism for the  
280 relationship between the north–south precipitation seesaw over CAWTP during both positive  
281 and negative NAO phases respectively. In the following, composite analysis was therefore  
282 used to further investigate how the different NAO phases influenced the regional circulation  
283 and precipitation over CAWTP.

284

## 285 **5 Influence of the NAO on spatial and temporal distribution of winter precipitation over** 286 **CAWTP**

287 Based on our definition of NAO events, the 500 hPa geopotential height, the 700 hPa wind  
288 flow field were combined to assess the influence of the NAO on the circulation over remote  
289 downstream areas. The time evolutions of composited 500hPa geopotential height anomaly  
290 and 700 hPa streamlines at different lags for the positive and negative NAO phase cases are  
291 illustrated in Fig. 6. In positive NAO phases, the NAO pattern is clearly shown on the 0 day (the  
292 peak day of NAO index) with the strong negative 500 hPa geopotential height anomaly over  
293 the Iceland and the positive one over the Azores. As time advances, the positive anomaly  
294 extends eastward to the Eurasian border. In the following days, NAO pattern is weakening and  
295 the east positive anomaly is further extended eastward and is finally separated from the

---

296 positive anomaly over the Azores. The eastward extension of positive anomaly over the  
297 Eurasian border is associated with the intensification of the negative anomaly over the CAWTP  
298 (Fig. 6c). The time evolutions of the 700 hPa wind streamlines associated with geopotential  
299 height anomaly evolutions offer another view. Associated with positive NAO at day 0 is a single  
300 strong westerly jet over the North Atlantic and two branches of strong westerly wind, whose  
301 axes locate on 55°N and 30°N along the Eurasian border, resulted from the positive 500 hPa  
302 geopotential height anomaly over the Eurasian border (Fig. 6a). Over the Eurasian border, the  
303 north branch westerly wind forms a ridge while the south one forms a trough. They both  
304 extend eastward in a similar way as the positive 500 hPa geopotential height anomaly. The  
305 north branch westerly wind goes around the north CAWTP while the south branch encounters  
306 the Karakoram Himalaya. The Figs. 6d, 6e and 6f show time evolutions of composited 500hPa  
307 geopotential height anomaly and 700 hPa streamlines at different days for the negative NAO  
308 phases. Time evolutions of geopotential height anomaly show similar evolutions as those  
309 during the positive NAO phase cases, but with a change in sign of the anomalies. Associated  
310 with the negative NAO phases, the north branch of westerly wind encounters the north  
311 CAWTP while the south branch goes around the Krakoram-Himalaya at day 10.

312 The time averaged 700 hPa moisture flux anomaly and WWD frequency anomaly from  
313 day 5 to day 10 after the peak of NAO phases intuitively show the regulation of regional  
314 circulation by the NAO. During the positive NAO phases, northeasterly moisture flux  
315 anomalies (decreased southwesterly moisture flux) occur over the Central Asia and northern  
316 Pamir Plateau, whereas southerly moisture flux anomalies accompanied with higher

---

317 frequency of WWD occur over the Karakoram Himalaya (Fig. 7a). During the negative NAO  
318 phases, southwesterly moisture flux anomalies occur over the Central Asia and northern  
319 Pamir Plateau, whereas northeasterly moisture flux anomalies accompanied with lower  
320 frequency of WWD occur over the Karakoram Himalaya (Fig. 7b). The composites of  
321 precipitation anomalies of positive and negative NAO phases, as shown in Fig. 7c and 7d, are  
322 well matched with the regional circulation and moisture flux anomalies. There is less  
323 precipitation over the north east of Iran, Turkmanistan, Tajikistan and Kyrgyzstan (center at ~  
324 75°E, 34°N) and more precipitation over the Karakoram Himalaya (center at ~ 70°E, 42°N)  
325 during positive NAO phases and vice versa. For the south part, the WWD seems to be more  
326 important while the moisture flux takes control of the north part. Compared with the daily  
327 average winter precipitation (Fig. 2a), the precipitation anomaly at the intraseasonal time  
328 scale reaches 10% of the climatological mean. The precipitation composites during the  
329 different NAO phases are similar to the results of the SVD analyses. The two analyses both  
330 demonstrate the teleconnection between the NAO over the North Atlantic and the regional  
331 circulation and precipitation variability over CAWTP.

332

## 333 **6 Discussion and conclusions**

334 The climate is characterized by dominant westerly circulation and scarce precipitation  
335 over CAWTP. The lowlands of this area are almost rainless due to the lack of moisture and  
336 upward motion. By contrast, heavy rains occur on the high mountain areas as a result of the  
337 uplifting of the westerly winds by the high topography.

---

338           There have been much published research on precipitation and its interannual variability  
339 over the Karakoram Himalaya (Syed et al. 2006, 2010, Filippi et al. 2014, Cannon et al. 2015a,  
340 b). For example, Cannon et al. (2015a, b) stressed the importance of the westerly disturbance.  
341 Less research has focused on precipitation over the northern Pamir Plateau and mainly  
342 focuses on interannual variations (e.g., Chen et al. 2011). Filippi et al. (2014) and Syed et al.  
343 (2006) found that the interannual variation in precipitation is connected to the NAO, but they  
344 did not discuss the intraseasonal precipitation variations and the contemporaneous opposite  
345 variations over the northern Pamir Plateau and over the Karakoram Himalaya.

346           This study focused on the intraseasonal variation in winter daily precipitation over CAWTP.  
347 The EOF, SVD, lead-lag linear regression and composite analyses showed that a seesaw pattern  
348 of winter intraseasonal precipitation anomaly between the Karakoram Himalaya and the  
349 northern Pamir Plateau is connected with the intraseasonal oscillation of the NAO. The main  
350 physical processes for the seasaw pattern of precipitation variability are the trough–ridge  
351 phase of the two westerly jets rather than the westerly strength at the intraseasonal scale.  
352 Multi-method analyses gave similar results, confirming that the NAO is able to influence the  
353 intraseasonal precipitation variability in winter over CAWTP.

354           The seesaw pattern of winter intraseasonal precipitation anomaly was found between  
355 the southeastern CAWTP (centered in the Karakoram Himalaya) and the northwestern CAWTP  
356 (centered in the northern Pamir Plateau) by the SVD analysis and this pattern of precipitation  
357 was closely connected to the regional 700 hPa circulation. When there was a northeasterly  
358 moisture flux anomaly (southwesterly moisture flux weakened) over the northwestern CAWTP

---

359 and a southwesterly moisture flux anomaly (southwesterly moisture flux strengthened) over  
360 the southwestern CAWTP at 700 hPa, a negative precipitation anomaly occurred over the  
361 northern Pamir Plateau and a positive anomaly over the Karakoram Himalaya. Accompanied  
362 by the seesaw precipitation pattern, a negative 500 hPa geopotential height anomaly over  
363 CAWTP (center located in the central Tibetan Plateau) was also observed, and vice versa.

364       The mechanism for the seesaw precipitation anomaly over CAWTP may be related to the  
365 NAO-like circulation at the intraseasonal time scale. The results of both the regression and  
366 composite analyses showed that the seesaw precipitation pattern was closely connected with  
367 the precursor NAO-like circulation anomalies over the North Atlantic. During the positive NAO  
368 phases, the southern branch of the 700 hPa westerly winds formed a ridge over the North  
369 Atlantic and combined with the northern branch which formed a trough. The two branches  
370 separated around Eurasian border. The southern branch then formed a trough over the Middle  
371 East, which increased the transport of moisture and the strength of the westerly winds over  
372 the Karakoram Himalaya. By contrast, the northern branch formed a ridge and went around  
373 the northwestern Tibetan Plateau, which decreased southwesterly winds, the southwesterly  
374 moisture transport, and therefore precipitation over the Central Asia and northern Pamir  
375 Plateau. The large scale wind stream pattern can modify the regional circulation. Meanwhile  
376 during positive NAO, more WWD occurred over the Karakoram Himalaya since south branch  
377 of westerly encounters the Himalaya, which finally increased the precipitation over Karakoram  
378 Himalaya. This pattern was reversed during the negative NAO phases. The main physical  
379 processes involved and discussed above for the influence of the NAO on the winter

---

380 precipitation variability at the intraseasonal time scale over CAWTP are illustrated in  
381 schematic diagrams of Fig. 8.

382

383 Acknowledgments. This work was jointly supported by the National Key Research and  
384 Development Program of China (2016YFA0601904) and the National Natural Science  
385 Foundation of China (41572150, 41690115). BD's contribution was funded by the UK-China  
386 Research & Innovation Partnership Fund through the Met Office Climate Science for Service  
387 Partnership (CSSP) China as part of the Newton Fund. The authors would like to thank an  
388 anonymous reviewer and editor Xianan Jiang for their constructive comments on the earlier  
389 version of the paper.

390

391

#### LITERATURE CITED

392 Aizen E M, Aizen V B, Melack J M and others (2001) Precipitation and atmospheric circulation  
393 patterns at mid-latitudes of Asia. *International Journal of Climatology* 21: 535-556

394 Bjornsson H, Venegas S A (1997) A manual for EOF and SVD analyses of climatic data.  
395 CCGCR Report97: 112-134

396 Bothe O, Fraedrich K, Zhu X (2012) Precipitation climate of Central Asia and the large-scale  
397 atmospheric circulation. *Theoretical and Applied Climatology*108: 345-354

398 Cannon F, Carvalho L M V, Jones C and others (2015a) Multi-annual variations in winter  
399 westerly disturbance activity affecting the Himalaya. *Climate Dynamics* 44: 441-455

400 Cannon F, Carvalho L M V, Jones C and others (2015b) Winter westerly disturbance dynamics

---

401 and precipitation in the western Himalaya and Karakoram: a wave-tracking approach.  
402 Theoretical and Applied Climatology: 1-18

403 Chen FH, Huang W, Jin LY, Chen J and others (2011) Spatiotemporal precipitation variations  
404 in the arid Central Asia in the context of global warming. Science China Earth Sciences  
405 54: 1812–1821

406 Chen M, Shi W, Xie P and others (2008) Assessing objective techniques for gauge-based  
407 analyses of global daily precipitation. Journal of Geophysical Research: Atmospheres 113:  
408 D04110, doi:10.1029/2007JD009132

409 Curio J, Maussion F, Scherer D (2015) A 12-year high-resolution climatology of atmospheric  
410 water transport over the Tibetan Plateau. Earth System Dynamics 6: 109-124

411 Dee D P, Uppala S M, Simmons A J and others (2011) The ERA-Interim reanalysis:  
412 Configuration and performance of the data assimilation system. Quarterly Journal of the  
413 Royal Meteorological Society 137: 553-597

414 Filippi L, Palazzi E, von Hardenberg J and others (2014) Multidecadal variations in the  
415 relationship between the NAO and winter precipitation in the Hindu Kush–Karakoram.  
416 Journal of Climate 27: 7890-7902

417 Guo H, Chen S, Bao A and others (2015) Inter-comparison of high-resolution satellite  
418 precipitation products over Central Asia. Remote Sensing 7: 7181-7211

419 Hoell A, Shukla S, Barlow M and others (2015) The forcing of monthly precipitation variability  
420 over Southwest Asia during the boreal cold season. Journal of Climate 28: 7038-7056

421 Hurrell, J W (1996) Decadal trends in the North Atlantic Oscillation: regional temperatures

---

422 and precipitation. *Geophysical Research Letters* 23: pp. 665–668

423 Lang T J, Barros A P (2004) Winter storms in the central Himalayas. *Journal of the*  
424 *Meteorological Society of Japan*82: 829-844

425 Malik K M, Taylor P A, Szeto K (2015) Characteristics of moisture flux convergence in Central  
426 Southwest Asia. *Theoretical and Applied Climatology* 120: 643-659

427 Mariotti A (2007) How ENSO impacts precipitation in southwest central Asia. *Geophysical*  
428 *Research Letters*34:L16706, doi:10.1029/2007GL030078

429 Maussion F, Scherer D, Mölg T and others (2014) Precipitation seasonality and variability over  
430 the Tibetan Plateau as resolved by the High Asia reanalysis. *Journal of Climate*27: 1910-  
431 1927

432 Ozturk T, Altinsoy H, Türkes M and others (2012) Simulation of temperature and precipitation  
433 climatology for the Central Asia CORDEX domain using RegCM 4.0. *Climate*  
434 *Research*52: 63-76

435 Pohl E, Gloaguen R, Seiler R (2015) Remote sensing-based assessment of the variability of  
436 winter and summer precipitation in the Pamirs and their effects on hydrology and hazards  
437 using harmonic time series analysis. *Remote Sensing*7: 9727-9752

438 Ragab R, Prudhomme C (2002) Climate change and water resources management in arid and  
439 semi-arid regions: prospective and challenges for the 21st century. *Biosystems*  
440 *Engineering* 81: 3-34

441 Rana S, McGregor J, Renwick J (2017) Wintertime precipitation climatology and ENSO  
442 sensitivity over central southwest Asia. *International Journal of Climatology* 37: 1494-

---

443 1509

444 Schiemann R, Lüthi D, Vidale P L and others (2008) The precipitation climate of Central  
445 Asia—intercomparison of observational and numerical data sources in a remote semiarid  
446 region. *International Journal of Climatology*28: 295-314

447 Schiemann R, Lüthi D, Schär C (2009) Seasonality and interannual variability of the westerly  
448 jet in the Tibetan Plateau region. *Journal of Climate* 22: 2940-2957

449 Small E E, Giorgi F, Sloan L C (1999) Regional climate model simulation of precipitation in  
450 central Asia: Mean and interannual variability. *Journal of Geophysical Research:*  
451 *Atmospheres*104(D6): 6563-6582

452 Syed F S, Giorgi F, Pal J S and others (2006) Effect of remote forcings on the winter  
453 precipitation of central southwest Asia part 1: observations. *Theoretical and Applied*  
454 *Climatology*86: 147-160

455 Syed F S, Giorgi F, Pal J S, et al. (2010) Regional climate model simulation of winter climate  
456 over Central–Southwest Asia, with emphasis on NAO and ENSO effects. *International*  
457 *Journal of Climatology*30(2): 220-235

458 Wallace J M, Smith C, Bretherton C S (1992) Singular value decomposition of wintertime sea  
459 surface temperature and 500-mb height anomalies. *Journal of Climate*5: 561-576

460 Wang N, Zhang Y (2015) Connections between the Eurasian teleconnection and concurrent  
461 variation of upper-level jets over East Asia. *Advances in Atmospheric Sciences*32: 336-  
462 348

463 WB, ISDR, CAREC (2009) Central Asia and Caucasus disaster risk management initiative

---

464 (CAC DRMI), Risk assessment for Central Asia and Caucasus. Desk study review: 1-  
465 155.[http://www.preventionweb.net/files/11641\\_CentralAsiaCaucasusDRManagementIni](http://www.preventionweb.net/files/11641_CentralAsiaCaucasusDRManagementInit.pdf)  
466 [t.pdf](http://www.preventionweb.net/files/11641_CentralAsiaCaucasusDRManagementInit.pdf) (accessed 15 Sep 2016)

467 Yadav R K, Rupa Kumar K, Rajeevan M. (2009) Increasing influence of ENSO and decreasing  
468 influence of AO/NAO in the recent decades over northwest India winter precipitation.  
469 *Journal of Geophysical Research: Atmospheres* 114(D12)

470 Yao J, Chen Y. (2015) Trend analysis of temperature and precipitation in the Syr Darya Basin  
471 in Central Asia. *Theoretical and Applied Climatology* 120(3-4): 521-531

472 Yin ZY, Wang HL, Liu XD (2014) A comparative study on precipitation climatology and  
473 interannual variability in subtropical East Asia and Central Asia. *Journal of Climate* 27:  
474 7830-7848  
475

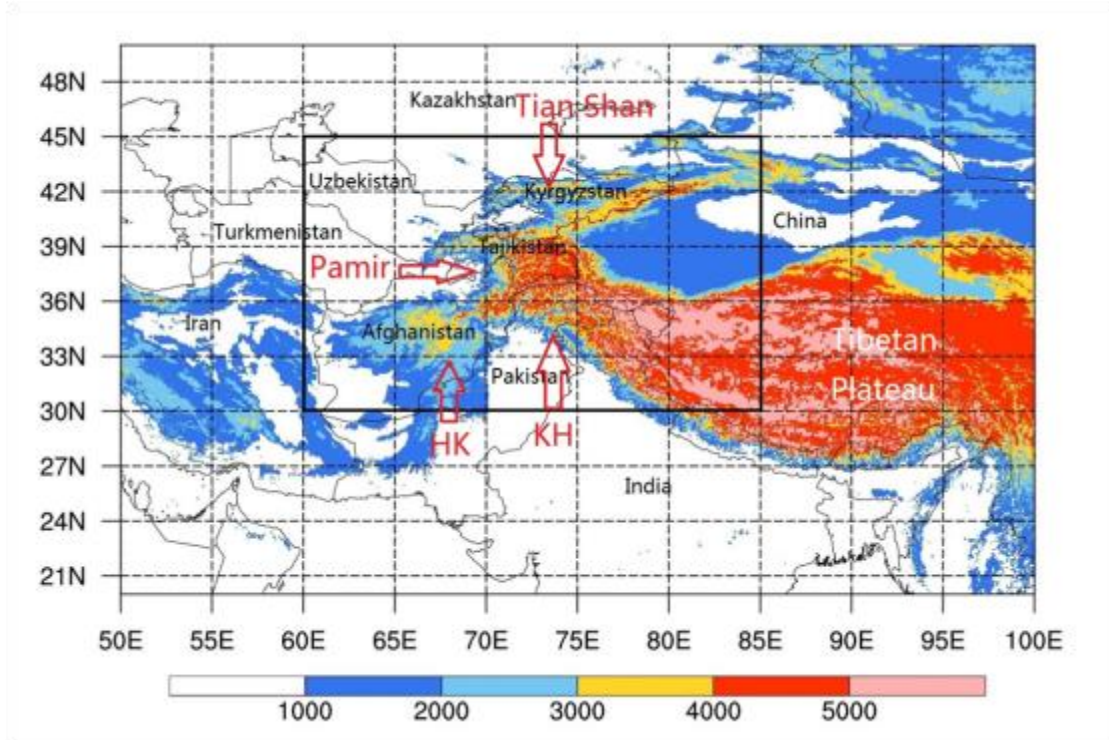
476 Table 1 Correlation coefficients of regionally-averaged 500 hPa geopotential heights on  
477 different lead-lag days for four regions indicated in Fig. 5 with the time coefficients of the  
478 first mode of 500 hPa geopotential height field over CAWTP in the SVD analysis mentioned in  
479 the text, and the correlation coefficients between NAO index and the time series. A negative  
480 lag means that the regionally-averaged height value over the four regions leads the height  
481 anomaly over CAWTP in the SVD analysis.

| Lag day | Area A | Area B  | Area C | Area D  | NAOI   |
|---------|--------|---------|--------|---------|--------|
| -16     | 0.13   | -0.14   | -0.06  | -0.15*  | 0.19** |
| -15     | 0.16*  | -0.22** | -0.01  | -0.20** | 0.22** |
| -14     | 0.17*  | -0.23** | 0.02   | -0.24** | 0.24** |
| -13     | 0.15*  | -0.24** | 0.04   | -0.26** | 0.24** |
| -12     | 0.14   | -0.30** | 0.07   | -0.29** | 0.23** |
| -11     | 0.13   | -0.33** | 0.11   | -0.30** | 0.21** |
| -10     | 0.15*  | -0.30** | 0.11   | -0.32** | 0.20** |
| -9      | 0.17*  | -0.32** | 0.11   | -0.35** | 0.20** |
| -8      | 0.14   | -0.36** | 0.10   | -0.38** | 0.21** |
| -7      | 0.13   | -0.44** | 0.11   | -0.41** | 0.20** |
| -6      | 0.17*  | -0.48** | 0.16   | -0.44** | 0.16*  |
| -5      | 0.20** | -0.46** | 0.26** | -0.47** | 0.12   |
| -4      | 0.17*  | -0.46** | 0.39** | -0.51** | 0.08   |
| -3      | 0.14   | -0.40** | 0.54** | -0.59** | 0.05   |
| -2      | 0.14   | -0.34** | 0.67** | -0.68** | 0.04   |
| -1      | 0.16*  | -0.23** | 0.70** | -0.75** | 0.04   |
| 0       | 0.15*  | -0.17*  | 0.67** | -0.67** | 0.00   |
| 1       | 0.12   | -0.16*  | 0.59** | -0.57** | -0.08  |
| 2       | 0.08   | -0.06   | 0.48** | -0.47** | -0.14  |
| 3       | 0.05   | -0.03   | 0.44** | -0.39** | -0.14  |

482 \*Significant at the 95% level

\*\*Significant at the 99% level

483

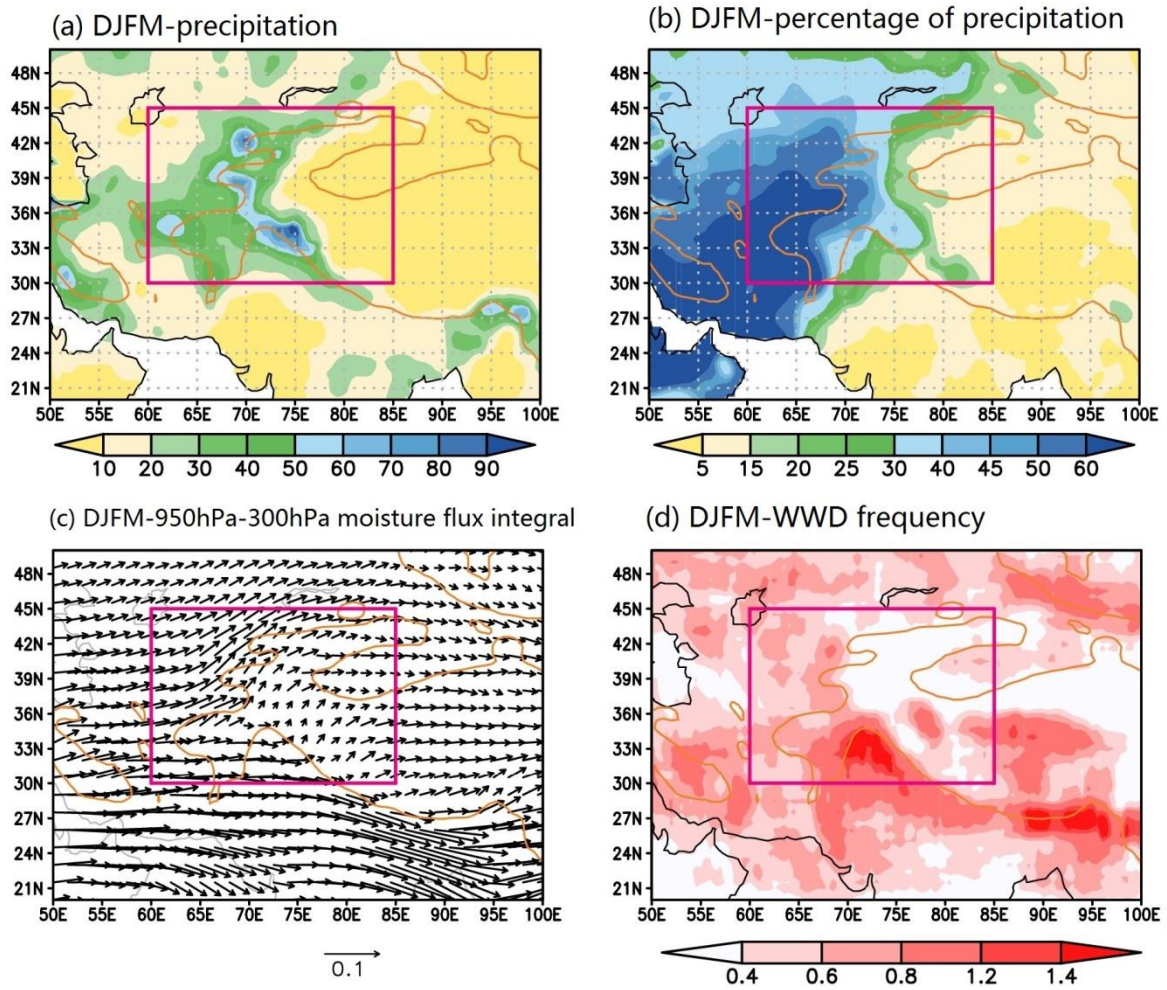


484

485 Fig. 1. Topography (color shaded areas, in meters) and national boundaries (thin gray lines) of

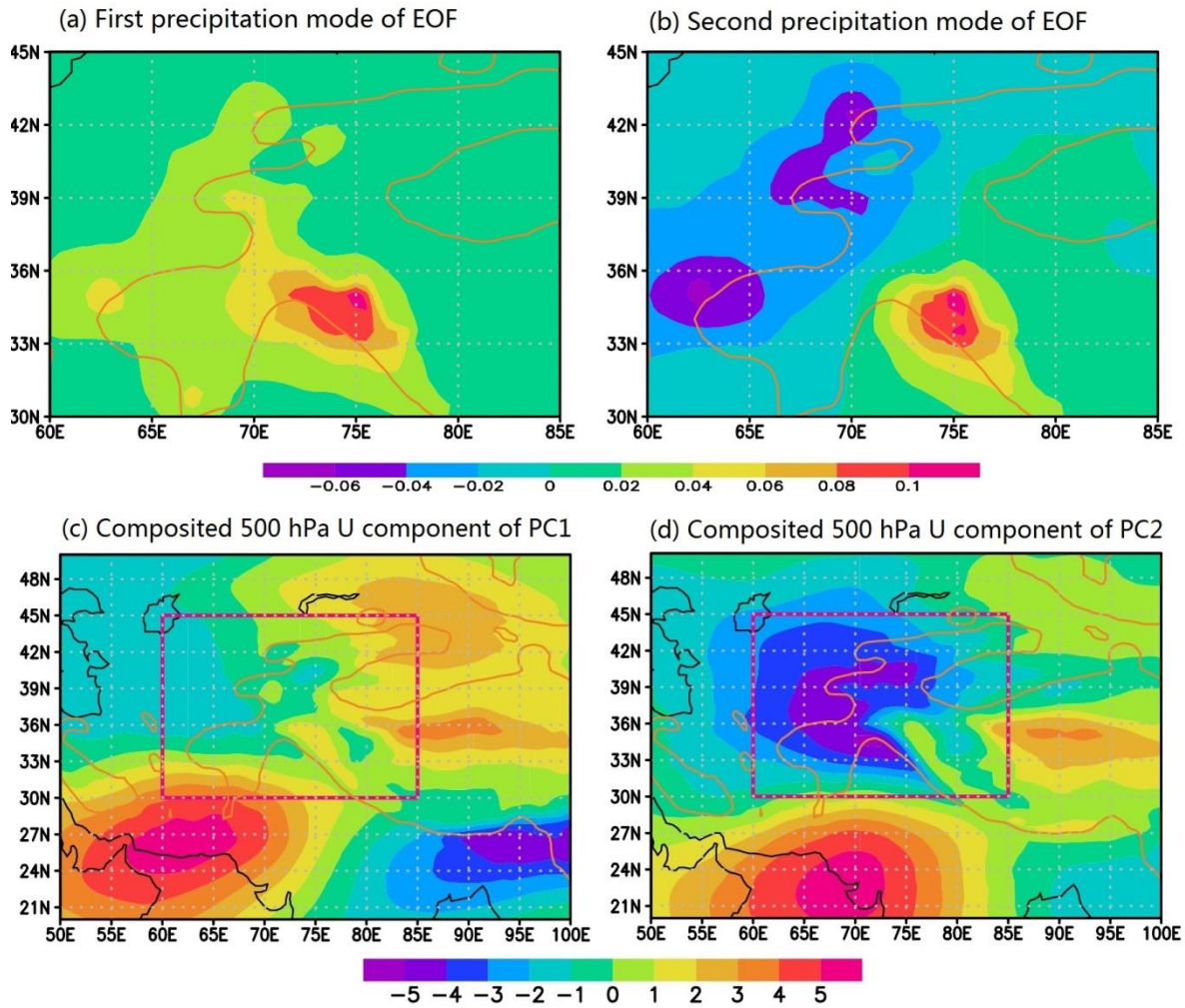
486 Central Asia, the western Tibetan Plateau (outlined by the black box) and surrounding areas.

487 HK and KH indicate Hindu Kush and Karakoram Himalaya, respectively.



488

489 Fig. 2. (a) Average precipitation ( $0.1 \text{ mm d}^{-1}$ ), (b) percentage of annual precipitation falling in  
 490 winter (%), (c) water vapor flux integrated vertically for 950–300 hPa ( $\text{kg m}^{-1} \text{ s}^{-1}$ ) and (d)  
 491 westerly wind disturbances frequency (percentage per day) in the CAWTP and surrounding  
 492 areas in winter (December–March) for 1979–2013. The brown lines indicate the topographic  
 493 contour of 1500 m and the red boxes represent the CAWTP region.

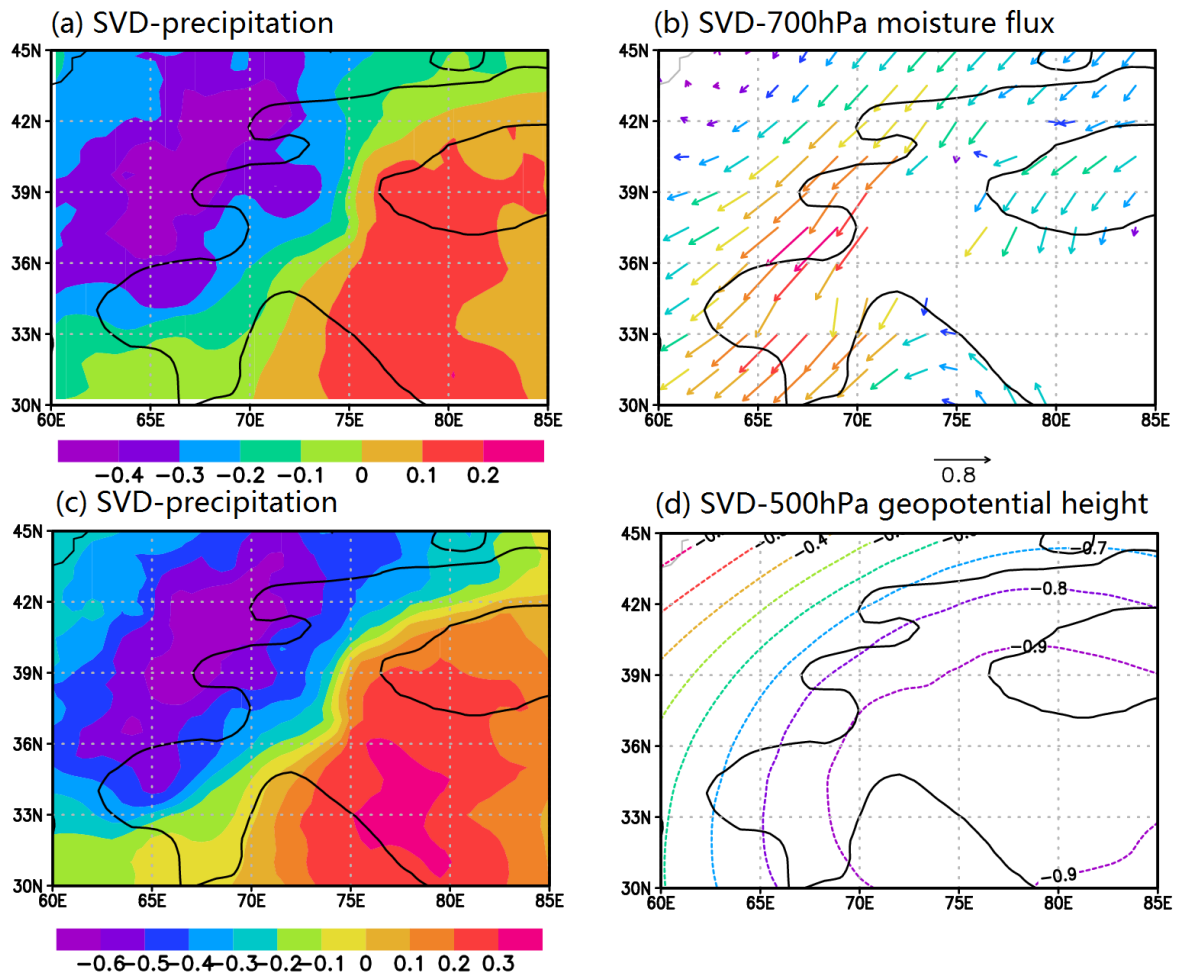


494

495 Fig. 3. First mode (a) and second mode (b) of the EOF analysis of daily precipitation field for  
 496 winters during 1979-2013. The composited 500 hPa zonal wind (U component) of the  
 497 dominant periods of the First mode (c) and second mode (d). The brown lines represent the  
 498 topographic contour of 1500 m.

499

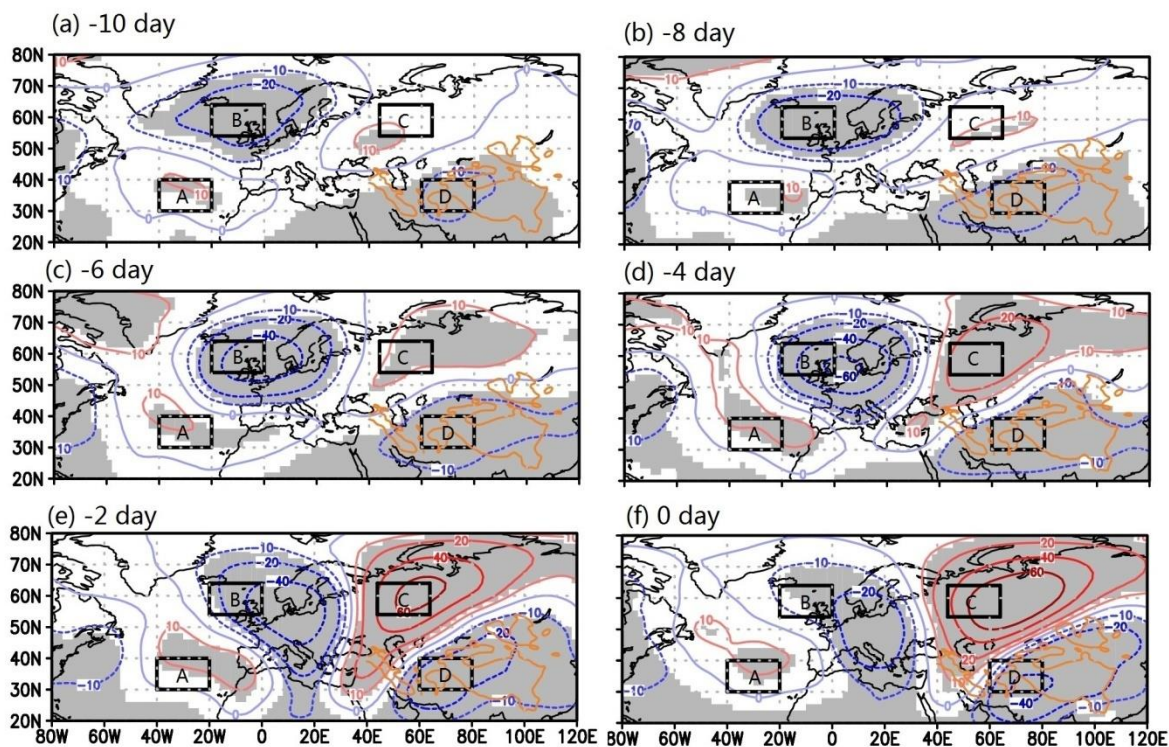
500



501

502 Fig. 4. First mode of the SVD analysis between seasonal cycle removed daily precipitation field  
503 (a) and 700 hPa daily moisture flux field (b) for winters during 1979-2013. Panels (c) and (d)  
504 are the same as (a) and (b), respectively, but for precipitation field (c) and 500 hPa  
505 geopotential height field (d). The black lines represent the topographic contour of 1500 m.

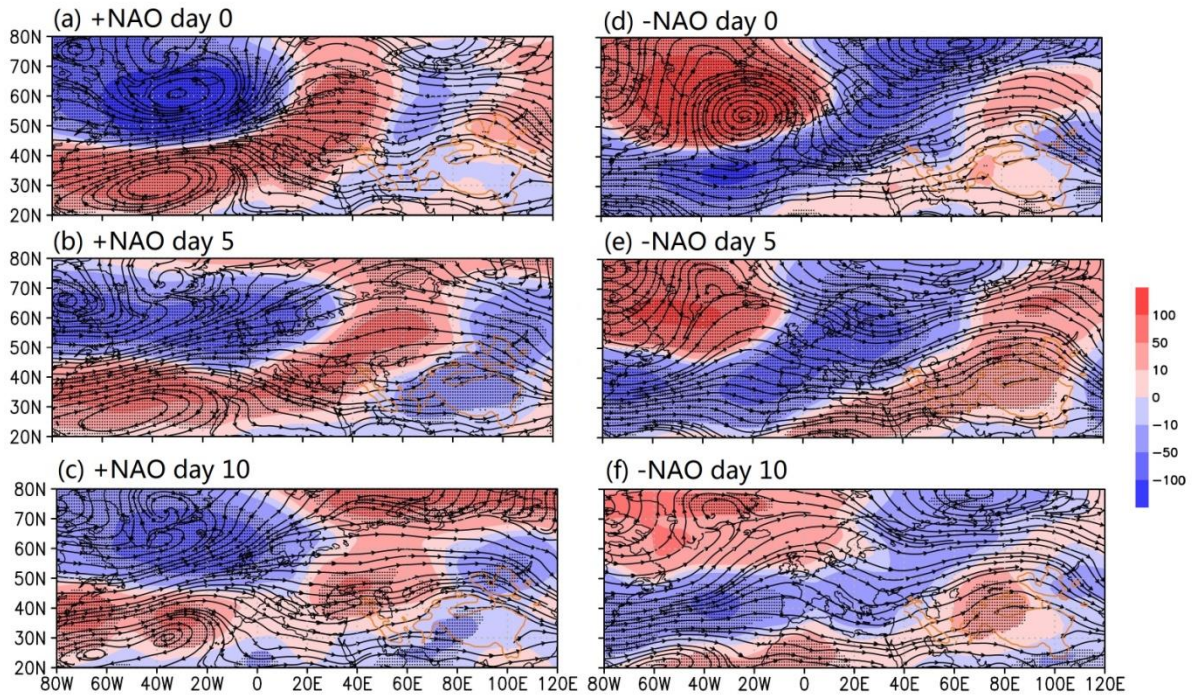
506



507

508 Fig. 5. Regressed 500hPa geopotential height anomaly fields for days (a) -10, (b) -8, (c) -6, (d)  
 509 -4, (e) -2 and (f) 0 with the chosen 200time coefficients of the first mode of 500 hPa  
 510 geopotential height field over CAWTP in the SVD analysis. The negative value indicates the  
 511 number of days before the day of SVD analysis. The contours represent the regression  
 512 coefficients and the gray shading represents the areas that were significant at the 95% level.  
 513 The brown lines represent the 1500 m topographic height and the black boxes represent the  
 514 four geopotential height anomaly centers.

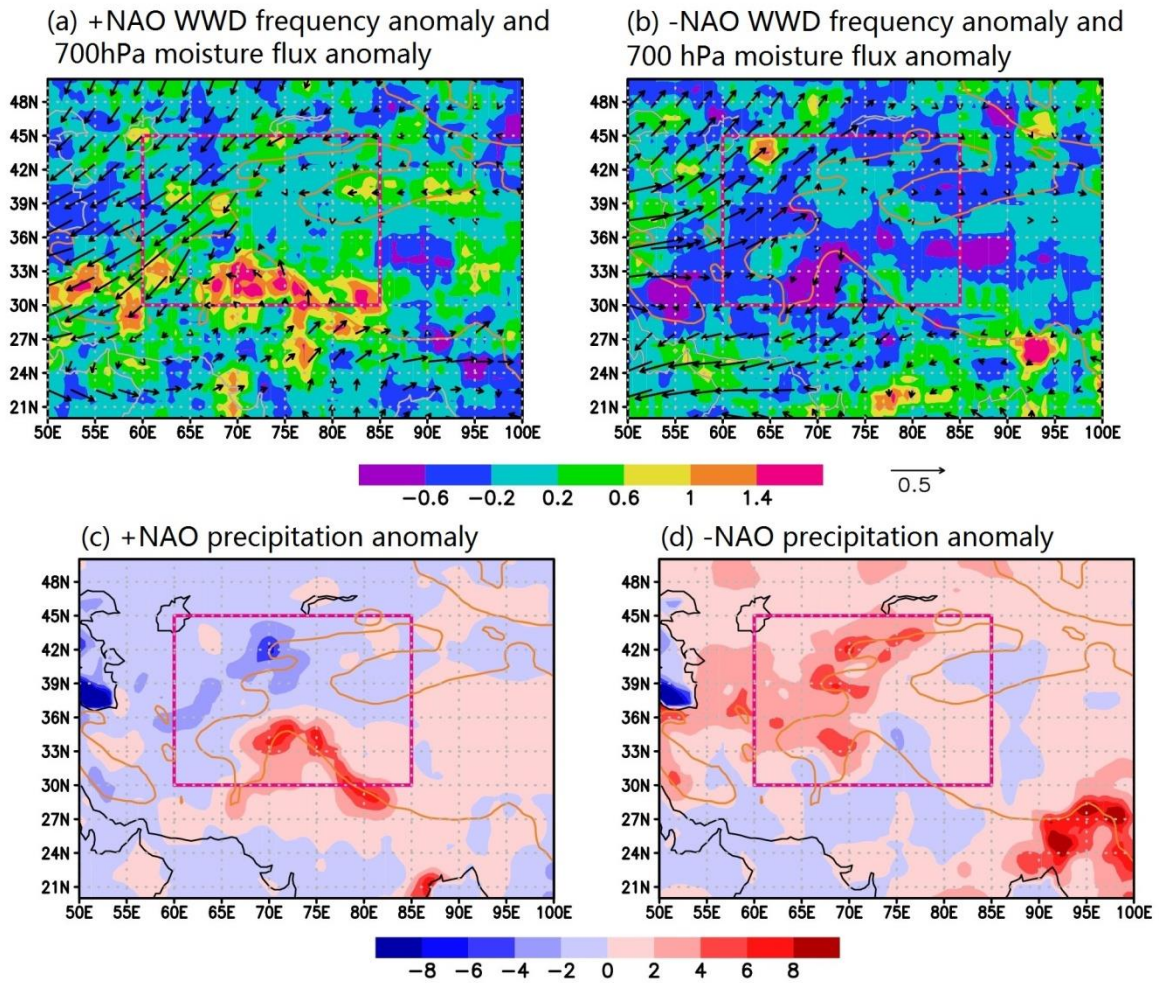
515



516

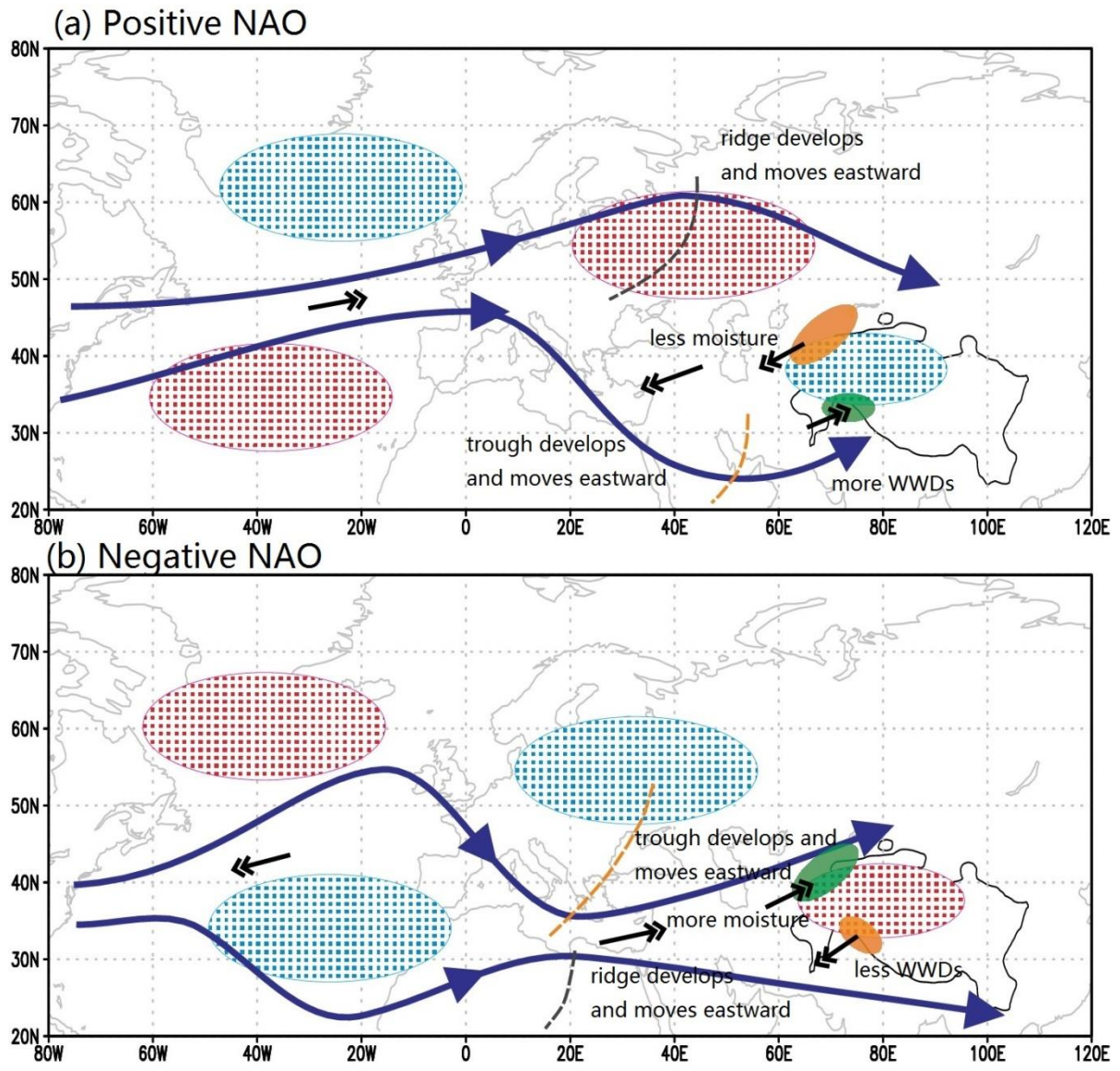
517 Fig. 6. The 500 hPa geopotential height anomaly (in potential meters) and 700 hPa wind  
 518 stream line averaged on the peak day (day 0), day 5 and lag day 10, composited for 85 positive  
 519 NAO events (a, b and c) and for 82 negative NAO events (d, e and f). The brown lines represent  
 520 the 1500 m isoheight. The dots represent the grid points where the 500 hPa geopotential  
 521 height anomaly were significant at the 95% significance level.

522



523

524 Fig. 7. The 700 hPa moisture flux anomaly ( $\text{g s}^{-1}\text{hPa}^{-1}\text{cm}^{-1}$ , vectors) averaged from +5 day (5  
 525 days after the peak day) to the +10 day and WWD frequency anomaly (percentage per day,  
 526 shaded), composited for 85 positive NAO events (a) and for 82 negative NAO events (b). Panels  
 527 (c) and (d) are the same as panels (a) and (b), respectively, but for precipitation anomaly (in  $0.1$   
 528  $\text{mm d}^{-1}$ ). The brown lines represent the 1500 m isoheight and the red boxes represent the  
 529 CAWTP region.



530

531 Fig. 8. Schematic diagrams showing how positive (a) and negative (b) NAO events influence  
 532 the precipitation over the CAWTP region. The red and blue ellipses are the areas of the 500  
 533 hPa positive and negative geopotential height anomalies. The blue lines represent the  
 534 southern and northern branches of the 700 hPa westerly circulation. The black arrows  
 535 represent the 700 hPa wind anomaly. The brown and gray dotted line represent troughs and  
 536 ridges. The green and yellow areas represent the positive and negative precipitation  
 537 anomalies.